

Semi-Empirical Model for Nano-Scale Device Simulations

Kurt Stokbro,* Dan Erik Petersen, Søren Smidstrup, Anders Blom, and Mads Ipsen
QuantumWise A/S,
Nørre Søgade 27A, 1. th,
DK-1370 Copenhagen K, Denmark

Kristen Kaasbjerg
Center for Atomic-scale Materials Design (CAMd),
Department of Physics, Technical University of Denmark,
DK-2800 Kgs. Lyngby, Denmark
(Dated: October 27, 2018)

We present a new semi-empirical model for calculating electron transport in atomic-scale devices. The model is an extension of the Extended Hückel method with a self-consistent Hartree potential. This potential models the effect of an external bias and corresponding charge re-arrangements in the device. It is also possible to include the effect of external gate potentials and continuum dielectric regions in the device. The model is used to study the electron transport through an organic molecule between gold surfaces, and it is demonstrated that the results are in closer agreement with experiments than *ab initio* approaches provide. In another example, we study the transition from tunneling to thermionic emission in a transistor structure based on graphene nanoribbons.

PACS numbers: 73.40.-c, 73.63.-b, 72.10.-d, 72.80.Vp

I. INTRODUCTION

As the minimum feature sizes of electronic devices are approaching the atomic scale, it becomes increasingly important to include the effects of single atoms in device simulations. In recent years, there have been several developments of atomic-scale electron transport simulation models based on the Non-Equilibrium Green's Function (NEGF) formalism¹. The approaches can roughly be divided into two categories: *ab initio* approaches, where the electronic structure of the system is calculated from first principles, typically with Density Functional Theory (DFT)²⁻⁵, and semi-empirical approaches, where the electronic structure is calculated using a model with adjustable parameters fitted to experiments or first-principles calculations. Examples of semi-empirical transport models are methods based on Slater-Koster tight-binding parameters^{6,7} and Extended Hückel parameters⁸⁻¹⁴.

The *ab initio* models have the advantage of predictive power, and can often give reasonable results for systems where there is no prior experimental data. However, the use of the Kohn-Sham one-particle states as quasiparticles is questionable, and it is well known that for many systems the energies of the unoccupied levels are rather poorly described within DFT. Furthermore, solving the Kohn-Sham equations can be computationally demanding, and solving for device structures with thousands of atoms is only feasible on large parallel computers.

The semi-empirical models have less predictive power, but when used within their application domain they can give very accurate results. The models may also be fitted to experimental data, and can thus in some cases give more accurate results than DFT-based methods. However, the main advantage of the semi-empirical methods

are their lower computational cost.

In this paper we will present the formalism behind a new semi-empirical transport model based on the Extended Hückel (EH) method. The model can be viewed as an extension to the work by Zahid *et al.*¹², with the main difference being the treatment of the electrostatic interactions. Zahid *et al.* only describe part of the electrostatic interactions in the device; most importantly, they use the Fermi level of the electrodes as a fitting parameter and do not account for the charge transfer from the electrodes to the device. In the current work, the Fermi level of the electrodes is determined self-consistently by using the methodology introduced by Brandbyge *et al.*⁴ In this way, we include the charge transfer from the electrodes to the device region and describe all electrostatic interactions self-consistently. This is accomplished by defining a real-space electron density and numerically solving for the Hartree potential on a real-space grid. Through a multi-grid Poisson solver, we include the self-consistent field from an applied bias, and allow for including continuum dielectric regions and electrostatic gates within the scattering region.

The organization of the paper is the following: In section II we introduce the self-consistent Extended Hückel (EH-SCF) model, and in section III we present the formalism for modelling nano-scale devices. In section IV we apply the model to a molecular device, and in section V we consider a graphene nano-transistor where an electrostatic gate is controlling the electron transport in the device. Finally, in section VI, we conclude the paper.

II. THE SELF-CONSISTENT EXTENDED-HÜCKEL METHOD

In this section we describe the EH-SCF framework. In Extended Hückel theory, the electronic structure of the system is expanded in a basis set of local atomic orbitals (LCAOs)

$$\phi_{nlm}(\mathbf{r}) = R_{nl}(r)Y_{lm}(\hat{r}), \quad (1)$$

where Y_{lm} is a spherical harmonic and R_{nl} is a superposition of Slater orbitals

$$R_{nl}(r) = \frac{r^{n-1-l}}{(2n)!} [C_1(2\eta_1)^{2n+1}e^{-\eta_1 r} + C_2(2\eta_2)^{2n+1}e^{-\eta_2 r}]. \quad (2)$$

The LCAOs are described by the adjustable parameters η_1 , η_2 , C_1 , and C_2 , and these parameters must be defined for the valence orbitals of each element.

The central object in EH theory is the overlap matrix,

$$S_{ij} = \begin{cases} \delta_{ij} & \text{if } \mathbf{R}_i = \mathbf{R}_j \\ \int_V \phi_i(\mathbf{r} - \mathbf{R}_i)\phi_j(\mathbf{r} - \mathbf{R}_j) d\mathbf{r} & \text{if } \mathbf{R}_i \neq \mathbf{R}_j \end{cases} \quad (3)$$

where i is a composite index for nlm and \mathbf{R}_i is the position of the center of orbital i .

From the overlap matrix, the one-electron Hamiltonian is defined by

$$H_{ij} = \begin{cases} E_i + \delta V_H(\mathbf{R}_i) & \text{if } i = j \\ \frac{1}{4}(\beta_i + \beta_j)(E_i + E_j)S_{ij} + \frac{1}{2}(\delta V_H(\mathbf{R}_i) + \delta V_H(\mathbf{R}_j))S_{ij} & \text{if } i \neq j \end{cases} \quad (4)$$

where E_i is an orbital energy, and β_i is an adjustable parameter (often chosen to be 1.75). $\delta V_H(\mathbf{R}_i)$ is the Hartree potential corresponding to the induced electron density on the atoms, i.e. the change in electron density compared to a superposition of neutral atomic-like densities. This term must be determined self-consistently, and is not included in standard EH models¹⁵. In the following section we describe how this term is calculated.

A. Solving the Poisson Equation to Obtain the Hartree Potential

To calculate the induced Hartree potential we need to determine the spatial distribution of the electron density. To this end, we introduce the Mulliken population of atom number μ

$$m_\mu = \sum_{i \in \mu} \sum_j D_{ij} S_{ij}, \quad (5)$$

where D_{ij} is the density matrix. The total number of electrons can now be written as a sum of atomic contributions, $N = \sum_\mu m_\mu$.

We will represent the spatial distribution of each atomic contribution by a Gaussian function, and use the

following approximation for the spatial distribution of the induced electron density:

$$\delta n(\mathbf{r}) = \sum_\mu \delta m_\mu \sqrt{\frac{\alpha_\mu}{\pi}} e^{-\alpha_\mu |\mathbf{r} - \mathbf{R}_\mu|^2}, \quad (6)$$

where the weight $\delta m_\mu = m_\mu - Z_\mu$ of each Gaussian is the excess charge of atom μ as obtained from the Mulliken population m_μ and the ion valence charge Z_μ . Subsequently, the Hartree potential is calculated from the Poisson equation

$$-\nabla \cdot [\epsilon(\mathbf{r}) \nabla \delta V_H(\mathbf{r})] = \delta n(\mathbf{r}), \quad (7)$$

which is solved with the appropriate boundary conditions on the leads and gate electrodes imposed by the applied voltages. Here, $\epsilon(\mathbf{r})$ is the spatially dependent dielectric constant of the device constituents, and allows for the inclusion of dielectric screening regions.

To see the significance of the width α_μ of the Gaussian orbital, let us calculate the electrostatic potential from a single Gaussian electron density at position \mathbf{R}_μ . The result is

$$\delta V_H(\mathbf{r}) = e(m_\mu - Z_\mu) \frac{\text{Erf}(\sqrt{\alpha_\mu} |\mathbf{r} - \mathbf{R}_\mu|)}{|\mathbf{r} - \mathbf{R}_\mu|}, \quad (8)$$

and from this equation we see that the on-site value of the Hartree potential is $\delta V_H(\mathbf{R}_\mu) = (m_\mu - Z_\mu)\gamma_\mu$, where the parameter

$$\gamma_\mu = 2e\sqrt{\frac{\alpha_\mu}{\pi}} \quad (9)$$

is the on-site Hartree shift. The parameter γ_μ is a well-known quantity in CNDO theory^{16,17}, and values of γ_μ are listed for many elements in the periodic table. Thus, we fix the value of γ_μ using CNDO theory, and then use Eq. (9) to calculate the value of α_μ for each element.

III. EH-SCF METHOD FOR A NANO-SCALE DEVICE

Fig. 1 illustrates the setup of a molecular device system. The system consists of three regions: the central region, and the left and right electrode regions. The central region includes the active parts of the device and sufficient parts of the contacts, such that the properties of the electrode regions can be described as bulk materials. For metallic contacts, this will typically be achieved by extending the central region 5–10 Å into the contacts.

The calculation of the electron transport properties of the system is divided into two parts. The first part is a self-consistent calculation for the electrodes, with periodic boundary conditions in the transport direction. In the directions perpendicular to the transport direction, we apply the same boundary conditions for the two electrodes and the central region, and these boundary conditions are described below.

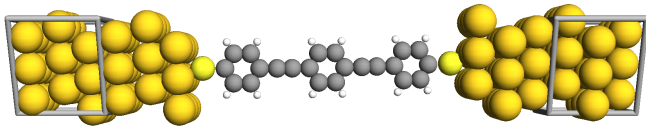


FIG. 1. (Color online) Geometry of a nano-device consisting of a dithiol-triethynylene-phenylene molecule attached to two (3x3) (111) gold electrodes. The left and right electrode regions are illustrated with wire boxes, and the properties of these regions are obtained from a calculation with periodic boundary conditions in all directions. The region between the two electrodes is the central device region, which is described with open boundary conditions in the transport direction, and periodic boundary conditions in the directions perpendicular to the transport direction.

In the second part of the calculation, the electrodes define the boundary conditions for a self-consistent open boundary calculation of the properties of the central region. The main steps in the open boundary calculation is the determination of the density matrix, the evaluation of the real-space density, and, finally, the calculation of the Hartree potential. These steps will be described in more detail in the following section.

A. Calculating the Self-Consistent Density Matrix of the Central Region

In this section we will describe the calculation of the density matrix of the central region. We assume that the self-consistent properties of the left and right electrodes have already been obtained, and thus we also know their respective Fermi levels, ε_L^F and ε_R^F . We allow for an external bias V_b to be applied between the two electrodes, and define the left and right chemical potentials $\mu_L = \varepsilon_L^F - eV_b$ and $\mu_R = \varepsilon_R^F$. The applied bias thus shifts all energies in the left electrode, and a positive bias gives rise to an electrical current from left to right.

The density matrix for this non-equilibrium system, with two different chemical potentials, is found by filling up the left and right originating states according to their respective chemical potentials^{4,18},

$$\hat{D} = \int_{-\infty}^{\infty} [\hat{\rho}^L(\varepsilon)n_F(\varepsilon - \mu_L) + \hat{\rho}^R(\varepsilon)n_F(\varepsilon - \mu_R)] d\varepsilon, \quad (10)$$

where $\hat{\rho}^L$ ($\hat{\rho}^R$) is the contribution to the spectral density of states from scattering states originating in the left (right) reservoir.

The calculation of the spectral densities is performed using NEGF theory, and we write the partial spectral densities as

$$\hat{\rho}^{L,R}(\varepsilon) = \frac{1}{2\pi} \hat{G}(\varepsilon) \hat{\Gamma}^{L,R}(\varepsilon) \hat{G}^\dagger(\varepsilon), \quad (11)$$

where \hat{G} is the retarded Green's function of the central region, and the broadening function $\hat{\Gamma} = i[\hat{\Sigma} - \hat{\Sigma}^\dagger]$ is given

by the self energies $\hat{\Sigma}^L$ and $\hat{\Sigma}^R$, which arise due to the coupling of the central region with the semi-infinite left and right electrodes, respectively.

Further details of the NEGF formalism can be found in Refs. 1,4. Here we just note that to improve the numerical efficiency, the integral in Eq. (10) is divided into an equilibrium and non-equilibrium part. The equilibrium part is calculated on a complex contour far from the real-axis poles of the Green's function, and only the non-equilibrium part is performed along the real axis. The equilibrium and non-equilibrium parts are then joined using the double-contour technique introduced by Brandbyge *et al.*⁴

From the density matrix we may now evaluate the real-space density in the central region using Eq. (6). It is important to note that near the left and right faces of the central region there will be contributions from the electrode regions, and this ‘‘spill in’’ must be properly accounted for.

Once the real-space density is known, the Hartree potential is calculated by solving the Poisson equation in Eq. (7) using a real-space multi-grid method. On the left and right faces of the central region the Hartree potential is fixed by the electrode Hartree potentials, appropriately shifted according to the applied bias. In the directions perpendicular to the transport directions, we apply the appropriate boundary conditions, fixed or periodic, as demanded by e.g. the presence of gate electrodes.

The so-obtained Hartree potential defines a new Hamiltonian, via Eq. 4, and the steps in section III A must be repeated until a self-consistent solution is obtained.

B. Transmission and Current

Once the self-consistent one-electron Hamiltonian has been obtained, we can finally evaluate the transmission coefficients^{1,19}

$$T(\varepsilon) = \text{Tr}[\hat{\Gamma}_L(\varepsilon)\hat{G}^\dagger(\varepsilon)\hat{\Gamma}_R(\varepsilon)\hat{G}(\varepsilon)] \quad (12)$$

and the current

$$I = \frac{2e}{h} \int_{-\infty}^{\infty} T(\varepsilon)[n_F(\varepsilon - \mu_L) - n_F(\varepsilon - \mu_R)] d\varepsilon. \quad (13)$$

In the following sections, we apply this formalism to the calculation of the electrical properties of a molecule between gold electrodes, as well as a graphene nano-transistor.

IV. TOUR WIRE BETWEEN GOLD ELECTRODES

In this section we will investigate the electrical properties of a phenylene ethynylene oligomer, also popularly

called a Tour wire. We will compare the electrical properties of the molecule when it is symmetrically and asymmetrically coupled with two Au(111) surfaces. In the symmetric system, as illustrated in Fig. 1, the molecule is connected with both gold surfaces through thiol bonds, whereas the asymmetric system only has a thiol bond to one of them.

The system has previously been investigated experimentally by Kushmerick *et al.*²⁰ and theoretically by Taylor *et al.*²¹, and it has been found that the asymmetrically coupled system shows strongly asymmetric I-V characteristics²⁰.

The calculations by Taylor *et al.* were based on DFT-LDA, and the asymmetric behaviour could be related to the voltage drop in the system. This system is therefore an excellent testing ground for our semi-empirical model, since a correct description of the electrical properties requires not only a good model for the zero-bias electronic structure, but also a good description of the bias-induced effects.

A. Transmission Spectrum of the Symmetric Tour Wire Junction

To setup the symmetric system we first relaxed the isolated Tour wire using DFT-LDA²². During the relaxation, passivating hydrogen atoms were kept on the sulfur atoms. Afterwards, these hydrogen atoms were removed and the two sulfur atoms placed at the FCC sites of two Au(111)-(3x3) surfaces. The height of the S atom above the surface was 1.9 Å (corresponding to an Au-S distance of 2.53 Å).

We next set up the EH model with Hoffmann parameters^{15,23} and perform a self-consistent calculation to obtain transmission spectra for different k-point sampling grids. The results are shown in the upper plot of Fig. 2. In each case, the same k-point grid was used for both the self-consistent and transmission calculation, and we see from the figure that using (1x1) k-point is insufficient while (2x2) and (4x4) k-points give almost identical results. Thus, we will use a (2x2) k-point sampling grid for the remainder of this study.

In the lower plot of Fig. 2 we compare the transmission spectra calculated with DFT-LDA, EH-SCF, and EH without the Hartree term of Eq. (4). For the DFT-LDA model we use similar parameters as Taylor *et al.*²¹, except for the k-point sampling which is (2x2) in the current study. The calculations in Ref. 21 were performed with a (1x1) k-point sampling, which is insufficient²⁴, and thus the DFT-LDA results in this study will differ from those by Taylor *et al.*

For the EH calculation we see a peak in the transmission spectrum just around the Fermi level of the gold electrodes. This peak arises from transmission through the LUMO orbital of the Tour wire.

In the self-consistent EH calculation there will be a charge transfer from the gold surface to the LUMO or-

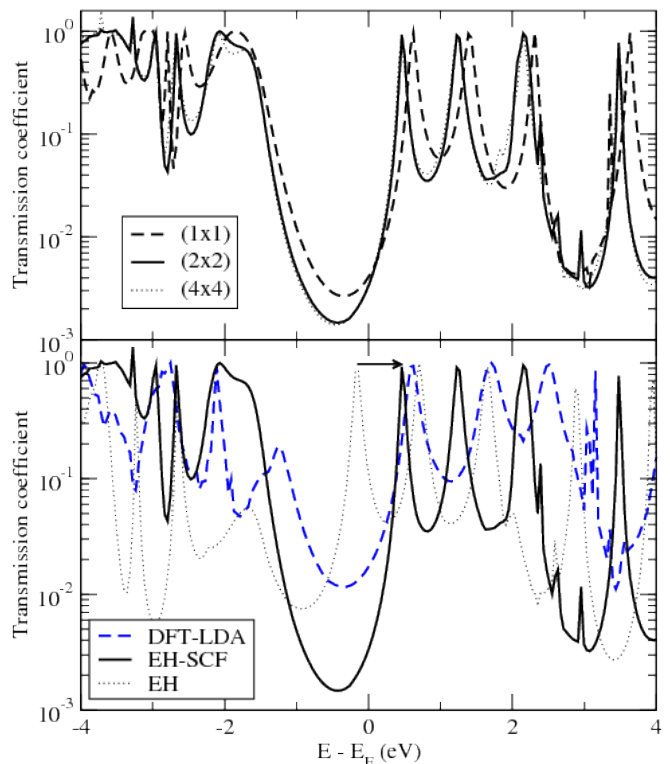


FIG. 2. (Color online) The upper plot shows the transmission spectrum of the symmetric Tour wire device, calculated with the EH-SCF model for three different k-point samplings. The lower plot shows transmission spectra calculated with a (2x2) k-point sampling using different models: EH-SCF (solid), EH without the Hartree term (dotted), and DFT-LDA (blue dashed). Energies are given relative to the Fermi level of the gold electrodes.

bital, and we see that this gives rise to a shift of the orbital by 1 eV, illustrated by the arrow in Fig. 2.

For the DFT-LDA calculation we see that the LUMO peak is shifted further away from the gold Fermi level, and the HOMO and LUMO peaks of the transmission spectrum are placed almost symmetrically around the gold Fermi level. We also note that the transmission coefficient at the Fermi level, corresponding to the zero-bias conductance, is almost one order of magnitude higher within the DFT-LDA model. We will discuss this further below.

We also note that Taylor *et al.* find a LUMO level even further away from the gold Fermi level; this is related to the insufficient k-point sampling.

B. I-V Characteristics of the Symmetric and Asymmetric Tour Wire Systems

We will now study both the symmetric and asymmetric Tour wire system and compare their respective I-V characteristics. The geometry of the asymmetric system

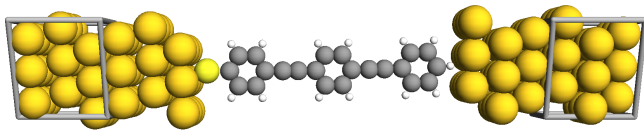


FIG. 3. (Color online) Geometry of the asymmetric system. The Tour wire is attached to the left gold electrode through a thiol bond, while the right end of the molecule is hydrogen-terminated and there is no chemical bond to the right gold electrode.

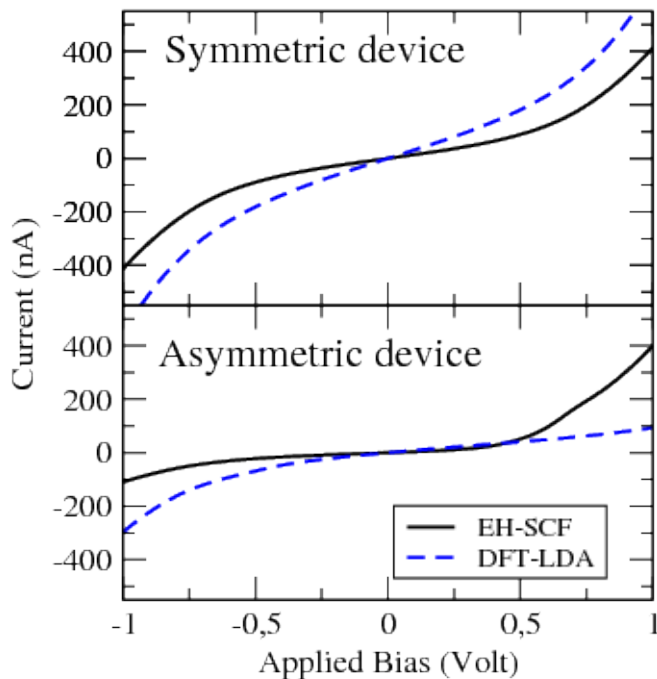


FIG. 4. (Color online) I-V characteristics of the symmetric (upper figure) and asymmetric (lower figure) Tour wire device. The positive current direction is from left to right.

is illustrated in Fig. 3. The geometry is similar to that of Fig. 1, except for the right-most sulfur atom which has been replaced by a hydrogen atom with a C-H bond length of 1.1 Å. The distance between the hydrogen atom and the right gold surface is 1.5 Å.

We perform self-consistent calculations for both the symmetric and asymmetric systems with the EH-SCF and DFT-LDA methods, and vary the bias from -1 to +1 V in steps of 0.1 V. The results are shown in Fig. 4. For the symmetric device we obtain rather similar, symmetric I-V characteristics for both the EH-SCF and DFT-LDA methods. The main difference is that the zero-bias conductance is significantly higher with DFT-LDA, reflecting the higher transmission coefficient at the Fermi level, as shown in Fig. 2.

For the asymmetric device we see that both the DFT-LDA and EH-SCF models give rise to rectification – how-

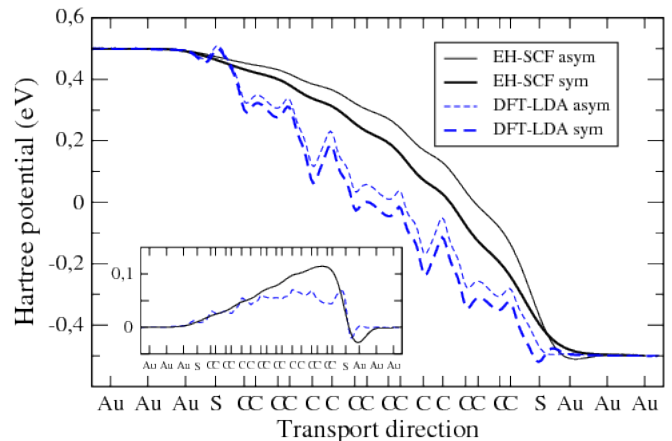


FIG. 5. (Color online) Voltage drop of the symmetric and asymmetric Tour wire systems along a line that goes through the two sulfur atoms in the symmetric system, for an applied bias of +1 V. The inset shows the voltage drop in the asymmetric system subtracted from the voltage drop in the symmetric system. Both plots show results calculated with the EH-SCF (solid) and DFT-LDA (dashed) models.

ever, in opposite directions. Taylor *et al.*²¹ demonstrated that the rectification was related to the voltage drop in the system, and we therefore in Fig. 5 compare the voltage drops obtained with the two methods. The EH-SCF voltage drop is smooth, since the charge density is composed of a superposition of single rather broad Gaussians on each atom. The DFT-LDA model shows atomic-scale details, however, as illustrated by the inset, the relative change in the voltage drop between the asymmetric and symmetric system is quite similar for the EH-SCF and DFT-LDA methods. Both methods reveal that in the asymmetric system there is an additional voltage drop at the contact with the weak bond. This is also one of the main results of Taylor *et al.*²¹.

The additional voltage drop at the weak contact means that the molecular levels of the Tour wire mainly follow the electrochemical potential of the right electrode²¹. Since the voltage drop is similar for the DFT-LDA and EH-SCF models, the difference in the I-V characteristics must be related to the different electronic structure at zero bias in the two models. Within the DFT-LDA model, the transport at the Fermi level is dominated by the HOMO. At negative bias, the left electrode has a higher electrochemical potential, and electrons from the occupied HOMO level can propagate to empty states in the left electrode. Thus, for the DFT-LDA model, the current is highest for a negative bias at the left electrode. For the EH-SCF model, on the other hand, the transport at the Fermi level is dominated by the LUMO, and the current in this case is highest for a positive bias at the left electrode.

Comparing with the experimental results of Kushmeric *et al.*²⁰, we find that the EH-SCF rectification direction agrees with the experimental rectification, while

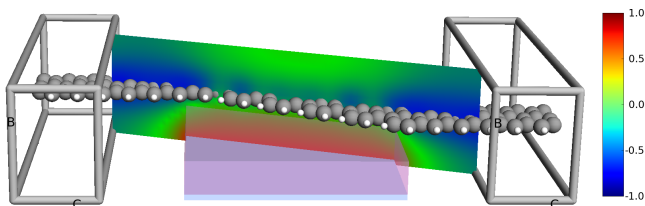


FIG. 6. (Color online) Graphene nano-transistor consisting of two metallic zigzag nanoribbons connected by a semiconducting armchair ribbon. The nanoribbons are passivated with hydrogen, and the width of the ribbons are 7 Å. The device is sitting on top of a dielectric and the transport is controlled by an electrostatic back-gate. The contour plot illustrates the Hartree potential for a gate potential of -1 V.

the DFT-LDA model predicts rectification in the opposite direction. We note that the rectification direction obtained with our DFT-LDA model is similar to the results of Taylor *et al.*²¹.

Thus, for this system it seems that the EH-SCF model is in better agreement with the experimental results, compared to the DFT-LDA model. The example shows that the EH-SCF model gives a very good description of both the electronic structure and the voltage drop in the system. The comparisons between the two methods also illustrates how small variations in the positions of the HOMO and LUMO levels may change the electrical properties of the Tour wire device.

V. Z-SHAPED GRAPHENE NANO-TRANSISTOR

In this section we will compare the electrical properties of a short (34 Å) and long (86 Å) graphene nano-transistor. The system consists of two electrodes consisting of metallic, zigzag-edge graphene nanoribbons connected through a semiconducting armchair-edge central ribbon. The system is placed 1.4 Å above a dielectric material with dielectric constant $\epsilon = 4\epsilon_0$, corresponding to SiO₂. The dielectric is 3 Å thick, and below the dielectric there is an electrostatic gate. The geometry of the short system is illustrated in Fig. 6. A similar system was investigated by Yan *et al.*²⁵ using DFT-LDA.

For the calculation we use EH parameters from Ref. 13 which were derived by fitting to a reference band structure of a graphene sheet calculated with DFT-LDA. With these parameters, we find a band gap of the central ribbon of 2.2 eV, in agreement with DFT-LDA calculations, which illustrates the transferability of the EH parameters from 2D graphene to a 1D graphene nanoribbon.

A. Transmission Spectrum

Fig. 7 shows the transmission spectrum for both the long and the short system when there is no applied bias

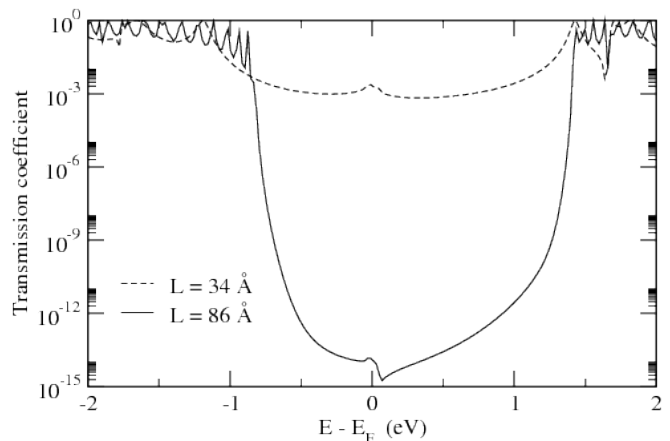


FIG. 7. Zero-bias transmission spectrum for the short (dashed) and long (solid) graphene device. Energies are relative to the Fermi level of the electrodes.

and zero gate potential. The shape of the transmission spectrum is directly related to the electronic structure of the central semiconducting ribbon.

The transmission is strongly reduced in the energy region from -0.7 to 1.5 eV, corresponding to the band gap of the central armchair ribbon. Since there are no energy levels in this interval, the electrons must tunnel in order to propagate across the junction. For the longer device the electrons must tunnel a longer distance, and thus the transmission is more strongly reduced.

Outside the band gap, the transmission is close to 1 and shows a number of oscillations. Since the central ribbon has a finite length, it resembles a molecule with a number of discrete energy levels. The levels give rise to peaks in the transmission spectrum, and since the longer system has more energy levels, the peaks are more closely spaced there.

In the following section we will see how this difference in the transmission spectrum gives rise to qualitatively different transport mechanisms in the two devices.

B. Transistor Characteristics

We now calculate the current for an applied source-drain voltage of 0.2 V as a function of the applied gate potential. Fig. 8 shows the current for the long and short devices, respectively, for gate potentials in the range -1 to 1 V, for different electrode temperatures. We see that for the short device there is only a small effect of the gate potential and electron temperature, while for the long device the conductance falls off exponentially, reaching a minimum in the range 0 to 0.5 V. Moreover, the current is strongly temperature-dependent.

The lack of temperature-dependence for the short device shows that the transport is completely dominated by electron tunneling. For the long device, on the

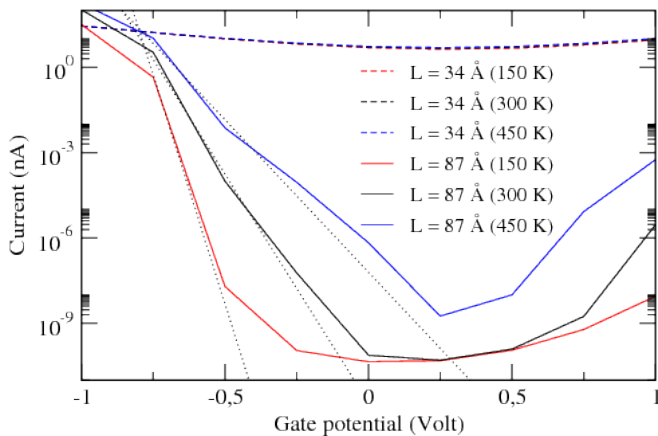


FIG. 8. (Color online) The tunneling current for a source-drain voltage of 0.2 V, as a function of the gate potential for the long (solid) and short (dashed) graphene device, respectively. Three different values of the electron temperature in the electrodes were considered: 150 K, 300 K and 450 K. The dotted lines illustrate the $1/k_B T$ slope for the different temperatures.

other hand, there is a strong temperature dependence, and in this case the electron transport is dominated by thermionic emission. The dotted lines illustrate the $1/k_B T$ slope expected for thermionic emission. We see that in the gate voltage range from -0.25 to -0.75 V, the I-V characteristics follow these slopes well.

Fig. 6 also shows the electrostatic profile through the device. We see that the gate potential is almost perfectly screened by the graphene ribbon, i.e. the gate potential does not penetrate through the central ribbon. This means that for a layered structure, only the first layer would be strongly affected by the back-gate. This has some implications also for gated nanotube devices. In such a device, only the atoms facing the gate electrode will be strongly influenced, and this explains why in Ref. 26 we found that the transport in the device was dominated by tunneling even though the nanotube was 110 Å long, and thus longer than the graphene junctions studied in this paper. Thus, to obtain efficient gating of a nanotube, the gate electrode must wrap around the tube.

VI. CONCLUSIONS

In this paper we have introduced a new semi-empirical model for electron transport in nano-devices. The model is based on the Extended Hückel method that extends the work by Zahid *et al.*¹² to give a more complete description of the electrostatic interactions in the device. In particular, the position of the electrode Fermi level and the charge transfer between the contacts and the device are calculated self-consistently.

Compared to DFT-based transport methods, the main advantage of our new method is that it is computationally less expensive, as well as having the option of adjusting parameters to reproduce experimental data or computationally very demanding many-body electronic structure methods.

The model includes a self-consistent Hartree potential which takes into account the effect of an external bias as well as continuum dielectric regions and external electrostatic gates.

We used the model to study a Tour wire between gold electrodes, and found that the voltage drop in the device compares well with *ab initio* results, while the calculated current-voltage characteristics qualitatively agree better with experimental findings than the corresponding DFT-LDA results do.

We also considered a graphene nano-transistor, and our study illustrated how the transport mechanism changes from tunnelling to thermionic emission as the device is made longer.

These applications show that the new method can give an accurate description of a broad range of nano-scale devices. With its favorable computational speed, it is a good complement to *ab initio*-based transport methods.

ACKNOWLEDGMENTS

This work was supported by the Danish Council for Strategic Research 'NABIIT' under Grant No. 2106-04-0017, "Parallel Algorithms for Computational Nano-Science", and European Commission STREP project No. MODECOM "NMP-CT-2006-016434", EU.

* <http://www.quantumwise.com>;
kurt.stokbro@quantumwise.com

¹ H. Haug and A.-P. Jauho, *Quantum Kinetics in Transport and Optics of Semiconductors* (Berlin Springer Verlag, 1996).

² N. D. Lang, Phys. Rev. B, **52**, 5335 (1995).

³ Y. Xue, Chemical Physics, **281**, 151 (2002).

⁴ M. Brandbyge, J.-L. Mozos, P. Ordejón, J. Taylor, and K. Stokbro, Phys. Rev. B, **65**, 165401 (2002).

⁵ J. Taylor, H. Guo, and J. Wang, Phys. Rev. B, **63**, 245407

(2001).

⁶ A. Di Carlo, Physica B, **314**, 211 (2002).

⁷ A. Pecchia and A. Di Carlo, Reports in Prog. in Phys., **67**, 1497 (2004).

⁸ M. Magoga and C. Joachim, Phys. Rev. B, **56**, 4722 (1997).

⁹ S. Corbel, J. Cerdá, and P. Sautet, Phys. Rev. B, **60**, 1989 (1999).

¹⁰ J. Cerdá and F. Soria, Phys. Rev. B, **61**, 7965 (2000).

¹¹ E. G. Emberly and G. Kirczenow, Phys. Rev. B, **62**, 10451 (2001).

- ¹² F. Zahid, M. Paulsson, E. Polizzi, A. W. Ghosh, L. Siddiqui, and S. Datta, *J. of Chem. Phys.*, **123**, 064707 (2005).
- ¹³ D. Kienle, J. I. Cerda, and A. W. Ghosh, *J. Appl. Phys.*, **100**, 043714 (2006).
- ¹⁴ D. Kienle, K. H. Bevan, G.-C. Liang, L. Siddiqui, J. I. Cerda, and A. W. Ghosh, *J. Appl. Phys.*, **100**, 043715 (2006).
- ¹⁵ M. H. Whangbo and R. Hoffmann, *J. Chem. Phys.*, **68**, 5498 (1978).
- ¹⁶ J. A. Pople and G. A. Segal, *J. Chem. Phys.*, **44**, 3289 (1966).
- ¹⁷ J. N. Murrell and A. J. Harget, *Semi-empirical SCF Theory of Molecules* (Wiley, 1972).
- ¹⁸ T. N. Todorov, J. Hoekstra, and A. P. Sutton, *Philos. Mag. B*, **80**, 421 (2000).
- ¹⁹ S. Datta, *Electronic Transport in Mesoscopic Systems* (Cambridge University Press, Cambridge, UK, 1997).
- ²⁰ J. G. Kushmerick, D. B. Holt, J. C. Yang, J. Naciri, M. H. Moore, and R. Shashidhar, *Phys. Rev. Lett.*, **89**, 86802 (2002).
- ²¹ J. Taylor, M. Brandbyge, and K. Stokbro, *Phys. Rev. Lett.*, **89**, 138301 (2002).
- ²² The transport calculations were performed with Atomistix ToolKit, version 2008.10. The manual is available online at <http://www.quantumwise.com/documents/manuals>.
- ²³ J. H. Ammeter, H. B. Burgi, J. C. Thibeault, and R. Hoffmann, *J. Am. Chem. Soc.*, **100**, 3686 (1978).
- ²⁴ K. S. Thygesen and K. W. Jacobsen, *Phys. Rev. B*, **72**, 033401 (2005).
- ²⁵ Q. Yan, B. Huang, J. Yu, F. Zheng, J. Zang, J. Wu, B.-L. Gu, F. Liu, and W. Duan, *Nano Letters*, **7**, 1489 (2007).
- ²⁶ H. H. B. Sørensen, P. C. Hansen, D. E. Petersen, S. Skelboe, and K. Stokbro, *Phys. Rev. B*, **79**, 205332 (2009).